scientific reports

Check for updates

OPEN

Magnetic moment impact on spin-dependent Seebeck coefficient of ferromagnetic thin films

Alain Portavoce[1]✉, Elie Assaf[1], Maxime Bertoglio[1], Dario Narducci[2] & Sylvain Bertaina[1]

Magnetic materials may be engineered to produce thermoelectric materials using spin-related effects. However, clear understanding of localized magnetic moments (μ_l), free carriers, and Seebeck coefficient (S) interrelations is mandatory for efficient material design. In this work, we investigate μ_l influence on the spin-dependent S of model ferromagnetic thin films, allowing μ_l thermal fluctuations, ordering, and density variation influence to be independently investigated. μ_l influence on free carrier polarization is found to be of highest importance on S: efficient coupling of free carrier spin and localized magnetic moment promotes the increase of S, while spin-dependent relaxation time difference between the two spin-dependent conduction channels leads to S decrease. Our observations support new routes for thermoelectric material design based on spin-related effects in ferromagnetic materials.

Energy saving is an important technological topic with many awaiting challenges, in particular in the case of the development of mobile technologies integrating a growing number of functionalities. Accompanying low-energy consumption device and high-power density battery development, energy harvesting technologies aim also at increasing portable electronic device autonomy[1–3]. Temperature gradients being usually present in microelectronic setups, integration of thermoelectric (TE) devices is currently explored[1,3]. TE solutions based on thin films compatible with the complementary-metal–oxide–semiconductor technology (CMOS) have already been proposed supporting TE device integration[4,5]. However, TE solutions for microelectronic applications need to operate close to room temperature (RT), TE efficiency being mainly dependent on intrinsic material properties, such as thermal conductivity (κ), electrical conductivity (σ), and Seebeck coefficient (S), TE technology improvement requires either the development of new materials, or to develop engineering methods allowing TE properties of current materials to be improved. Concurrent with κ engineering, recent band engineering solutions were proposed to increase the TE power factor $PF = S^2\sigma$[6], such as modulation doping[7,8], resonance levels[9,10], energy filtering[11–13], and quantum confinement[14]. The thermopower S is related to the Peltier coefficient Π such as $S = \Pi/T$, Π corresponding to the energy carried by the mobile charge carriers in the material per unit of charge. Figure 1a presents the method used for the measurement of $S = \Delta V/\Delta T$. Semiconductor materials are extensively studied[15–18], as a same semiconductor can be used as n-type or p-type TE material depending on doping, and they allow substantial band engineering. However, interest of spin effects on material TE properties is growing, and investigations on magnetic material potential for TE applications has considerably raised. In particular, the spin-Seebeck effect offers new routes for converting waste heat to electric power[19]. Based on spin transport, spin-Seebeck was demonstrated in different types of ferromagnetic materials: metallic[20], semiconductor[21], and insulator[22]. Investigations of magnetism influence on material TE performance have been reported[23], and original ferromagnetic materials[23–25] and spintronic structures[24,26] have been proposed for TE energy harvesting. Spin effects on the conventional Seebeck coefficient were shown to provide interesting ways of S engineering, based on charge carrier interactions with localized magnetic moments through the magnon-drag effect[27] or the spin fluctuation effect[28], for example. Thus, spin effect engineering in ferromagnetic (FM) materials should be considered as a possible way of obtaining improved TE properties, and interactions of mobile charge carriers with localized magnetic moments should be thoroughly investigated.

[1]IM2NP, Aix-Marseille University/CNRS, Faculté des Sciences de Saint-Jérôme case 142, 13397 Marseille, France. [2]Department of Materials Science, University of Milano-Bicocca, Via R. Cozzi 55, 20125 Milan, Italy. ✉email: alain.portavoce@im2np.fr

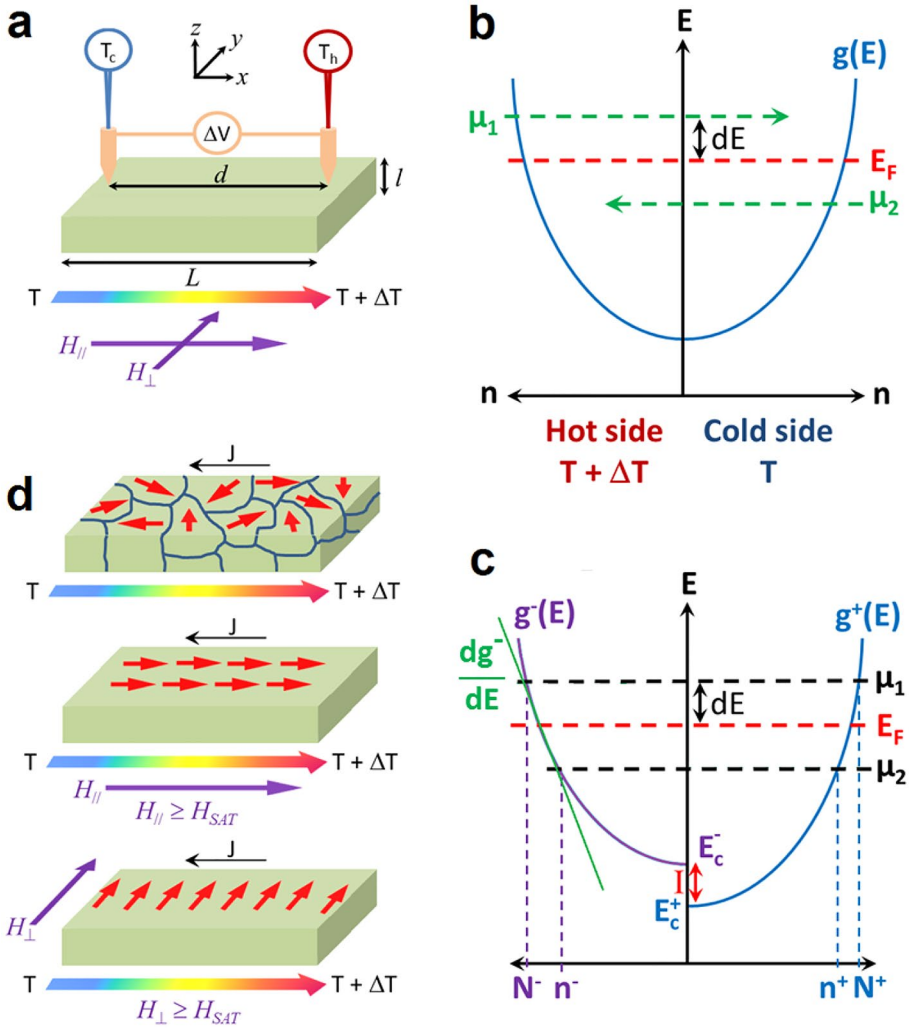

Figure 1. Schematics of *S* measurements in FM thin films and schematics of electronic DOS in PM and FM metallic materials under temperature gradient. (**a**) *S* measurement principle. (**b**) DOS of a PM metallic-type material under temperature gradient. (**c**) DOS of a FM metallic-type material under temperature gradient. (**d**) $\boldsymbol{\mu_I}$ distribution in a FM thin film under temperature gradient without magnetic field, or at saturation with a parallel ($H_{//}$) or perpendicular ($H_\perp$) magnetic field.

In this work, the influence of interactions between localized magnetic moments and spin-polarized free electrons on the spin-dependent Seebeck coefficient is investigated in FM thin films exhibiting metallic conduction and low charge carrier density. In order to separate as much as possible the effects of magnetic moment fluctuation, ordering, and density, the investigations focus on two FM germanides Mn_5Ge_3[29–34] and MnCoGe[35–43], with magnetization ($\boldsymbol{M}$) depending on a single element (almost single magnetic moment $\boldsymbol{\mu_I}$ carried by Mn ions, Supplementary Fig. S1), and exhibiting Curie temperatures (T_c) close to RT, allowing *S* measurements and *M* variations at T_c to be compared in the same temperature range. The film geometry allows $\boldsymbol{\mu_I}$ degree of freedom to be reduced, as the moments are forced to be aligned in the film plane[42,44].

Spin-dependent Seebeck coefficient. In the following, the term spin-dependent Seebeck coefficient is used to designate the regular Seebeck coefficient measured in FM materials below the Curie temperature. For paramagnetic (PM) metallic materials in a temperature gradient, *S* depends on the asymmetry of a single density of states (DOS) $g(E)$ close to the average Fermi level (E_F) corresponding to the considered temperature gradient (Fig. 1b). The average electrochemical potential (μ_1) of electrons above E_F promotes the diffusion of electrons towards the sample's cold side, while the average electrochemical potential (μ_2) of electrons below E_F promotes the diffusion of electrons towards the sample's hot side (Fig. 1b), due to the difference of electronic state filling between the two sides.

The net electron flux is given by the difference between these two fluxes, and leads to the accumulation of electrons at one side of the sample and immobile matrix ions at the other side of the sample, building the potential difference $\Delta V = -(\mu_1 - \mu_2)/e$ (e is the elementary charge). The Seebeck coefficient can be expressed as:

$$S = -\Delta\mu/eT, \tag{1}$$

with $\Delta\mu = \mu_1 - \mu_2$ (Fig. 1b). However, S depends on the asymmetry of the two DOS $g^+(E)$ and $g^-(E)$ of respectively majority-spin and minority-spin electrons (Fig. 1c), leading to two separate electronic currents in the case of FM materials: (i) the current of majority-spin electrons related to $g^+(E)$ and the electron densities N^+ above E_F and n^+ below E_F, as well as (ii) the current of minority-spin electrons related to $g^-(E)$ and the electron densities N^- above E_F and n^- below E_F. In this case $\Delta\mu = \Delta\mu^+ + \Delta\mu^-$ in Eq. 1, with $\Delta\mu^+ = \mu_1{}^+ - \mu_2{}^+$ and $\Delta\mu^- = \mu_1{}^- - \mu_2{}^-$. Considering the simplified model presented in Fig. 1c, S can be expressed as

$$S = -\frac{1}{2eT}\frac{d\varepsilon}{n}\left[\left(\frac{dg^+}{d\epsilon}\right)_{E_F} - \left(\frac{dg^-}{d\epsilon}\right)_{E_F}\right](\Delta E_C + \alpha\Delta E_{eI} + \Delta R k_B T), \tag{2}$$

considering that the FM material of interest reports a relatively low density of carriers[45]. The carrier density in the considered Mn_5Ge_3 and MnCoGe films is respectively 1.6×10^{20} cm^{-3} and 1.7×10^{18} cm^{-3} according to RT Hall effect measurements. $d\varepsilon$ is the energy variation around E_F involved with the temperature gradient, and $n = n^+ + n^-$ is the entire number of electronic state close to E_F (below E_F according to Fig. 1c). $\Delta E_C = E_C{}^- - E_C{}^+ = I$ in Fig. 1c corresponds to the energy difference between the bottom energies $E_C{}^-$ and $E_C{}^+$ of the conduction bands of the minority-spin and majority-spin electrons, respectively. $\Delta E_{eI} = E_{eI}{}^- - E_{eI}{}^+$ with $E_{eI}{}^j$ the average energy related to the polarization of the magnetic moment of conduction electrons of spin polarization j by the localized magnetic moments. This parameter does not consider macroscopic effects, such as those due to magnetic domains' walls for example. Thus, the parameter α is added in order to take into account a statistical efficiency of free electron polarization. $\Delta R = R^+ - R^-$ with R^j a dimensionless constant related to the average energy of electrons of spin polarization j depending on scattering mechanisms[46,47]. Considering that at given T $(dg^+/d\varepsilon)_{EF} = \Omega^+$ and $(dg^-/d\varepsilon)_{EF} = \Omega^-$, one can define a parameter $\beta(T) = d\varepsilon/n\ (\Omega^+ - \Omega^-)$. In this case

$$S = -\frac{\beta}{2eT}(\Delta E_C + \alpha\Delta E_{eI} + \Delta R k_B T). \tag{3}$$

Localized magnetic moment fluctuation. The diffractogram (a) in Fig. 2a was acquired on the Mn_5Ge_3 film (Supplementary Fig. S1a). The film is polycrystalline and the Scherrer equation[48] applied to the most intense diffraction peak $Mn_5Ge_3(211)$ indicates that the layer is composed of columnar grains with a thickness ~ 49 ± 5 nm. Grains exhibit an average lateral size ~ 1 µm and the root mean square (RMS) surface roughness of the film is ~ 1.8 nm according to AFM measurements[44]. Figure 3a shows the variation of the Mn_5Ge_3 film magnetization versus temperature in the temperature range $175 \le T \le 350$ K. M decreases as temperature increases up to the Curie temperature of the FM/PM transition at $T_c = 297$ K. The Curie temperature corresponds to the carbon-free Mn_5Ge_3 compound[49]. The electrical conductivity variation of the sample versus T is presented in the inset. The conductivity decreases almost linearly when the temperature increases from 150 K up to T_c. Figure 3b displays the variations of the spin-dependent S of the layer in the same temperature range. The black line corresponds to measurements performed without external magnetic field. The Mn_5Ge_3 film was not exposed to any magnetic field before Seebeck measurements. Consequently, the net magnetization is essentially zero in these conditions. The gray envelop around the data corresponds to the maximum measurement error observed on S in this study. This error considers both elaboration and Seebeck measurement reproducibility. It is only shown on this measurement for clarity.

Mn_5Ge_3 is n-type as $S < 0$. S decreases as temperature below the FM/PM transition increases, following a linear behavior from $T \sim 215$ K to $T = T_c$. Remarkably, S and σ are found to concurrently increase as temperature decreases, leading to a PF increase > 1700% from 300 to 175 K. Without external field, the Mn_5Ge_3 film exhibits weak magnetization due to moment disorder and fluctuations, in particular at RT close to T_c. However, magnetic domains (~ 0.65×1.5 µm^2) as depicted in Fig. 1d can still be observed in the film at that temperature by magnetic force microscopy[44].

When the temperature increases towards T_c, the fluctuation of localized moments increases and the distribution of the $\boldsymbol{\mu_I}$ orientations increases: the size of the magnetic domains decreases and the density of magnetic domain walls increases. The magnetization of the film decreases at the same time, in a similar way as observed in Fig. 3a. S decreases linearly during this process (Fig. 3b). Constant parameters A and B were determined experimentally from the measurements presented in Fig. 3b, considering[47]

$$S = -\frac{1}{eT}(A + Bk_B T). \tag{4}$$

They are reported in Table 1. Assuming that ΔE_C is negligible for Mn_5Ge_3[31,34] and combining Eqs. (3) and (4) one obtains $A = \beta\alpha\Delta E_{eI}/2$ and $B = \beta\Delta R/2$. Consequently, the linear behavior of S versus T suggests that the localized moment fluctuation effect occurs at constant β, constant $\alpha\Delta E_{eI}$, and constant ΔR, with $\beta\alpha\Delta E_{eI} = 0.01$ eV and $\beta\Delta R \sim -1/3$. β depends on the DOS of spin-up and spin-down electrons (Fig. 1c) and should a priori vary with temperature. However, the energy variation related to a temperature change from 200 to 300 K is only ~ 8.62×10^{-3} eV, which may explain that the parameter β is found to be almost constant in our temperature range of investigation. ΔE_{eI} is related to the energy gain involved with the polarization of free electrons by the magnetic moments localized on Mn ions. Considering that electron spin-up $s_e{}^+ = +½$ and electron spin-down $s_e{}^- = -½$, $\Delta E_{eI} = ½\ (J_{eI}{}^+ + J_{eI}{}^-)\mu_I \cos\theta$, with $J_{eI}{}^j$ the exchange parameter of spin-up electrons (j = '+') or of spin-down electrons (j = '−'), and θ the angle between the localized moment and the electron spin. $J_{eI}{}^j$ and μ_I are expected

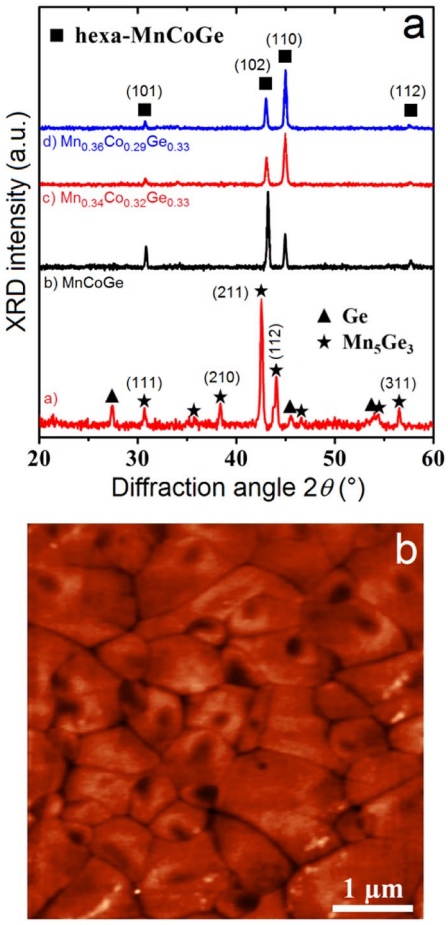

Figure 2. Microstructures of the 50 nm-thick Mn_5Ge_3 film and of the 150 nm-thick $Mn_xCo_yGe_{1-x-y}$ films. (**a**) X-ray diffractograms measured on Mn_5Ge_3 and $Mn_xCo_yGe_{1-x-y}$ films. (**b**) AFM measurements performed on the film MnCoGe.

to be independent of T in this model, and θ can be fixed to $\theta = 0$ since ΔE_{eI} corresponds to an average energy. Thus, ΔE_{eI} should indeed be independent of T. α is also found to be independent of μ_I fluctuations with T close to T_c in Mn_5Ge_3. ΔR is related to the spin-dependence of free carrier scattering mechanisms. Indeed, the free carrier relaxation time τ is expected to be spin-dependent in FM materials, which is responsible for free carrier polarization $P = (\gamma - 1)/(\gamma + 1)$ with $\gamma = \tau^+/\tau^-$. In our case, both Mn ions[50] and magnetic domain walls can act as spin-dependent scattering centers[51,52].

Thermal fluctuations of localized magnetic moments lead to the decrease of the spin-dependent S along with magnetization (and polarization). The increase of the product $\beta\alpha\Delta E_{eI}$ promotes the increase of S, while the increase of the product $\beta\Delta R$ leads to a decrease of S, since $A > 0$ and $B < 0$ (Table 1).

Magnetic moment ordering. Mn_5Ge_3 spin-dependent S variations versus temperature were also studied under an external magnetic field $\boldsymbol{H}$ applied in the film plane as shown in Fig. 1a. Figure 3b presents S variations versus temperature for four different magnetic field intensities $H^{//} = 8.6 \times 10^{-3}$, 27×10^{-3}, 46×10^{-3}, and 73×10^{-3} Tesla in the direction parallel to the temperature gradient (Fig. 1a), as well as S measurements performed under an external magnetic field either oriented at 45° ($H_4^{45°} = 73 \times 10^{-3}$ T), 90° ($H_5^{\perp} = 110 \times 10^{-3}$ T), 135° ($H_4^{135°} = 73 \times 10^{-3}$ T), and 180° ($H_3^{180°} = 46 \times 10^{-3}$ T) compared to the temperature gradient direction (Fig. 1a). S variations versus temperature in presence of $\boldsymbol{H}$ are again found to be linear up to the FM/PA transition. The external magnetic field $\boldsymbol{H}$ promotes the increase of S at constant T, but the in-plane field effect is independent of the field direction and of the field intensity. Figure 3c shows the magnetization variations of the Mn_5Ge_3 film versus in-plane magnetic field intensity measured at 270 K (blue dashed line) and 200 K (solid squares). According to the magnetic hysteresis loop, the film magnetization was at saturation for all the S measurements performed under external magnetic field ($H = H_{SAT}$), which can explain $\boldsymbol{H}$ effect on S to be independent of $\boldsymbol{H}$ intensity and orientation, considering the influence of the external field to be related to localized moment ordering and magnetic domain wall density variations (Fig. 1d). Maximum polarization of conduction electrons being reached at magnetization saturation, one should consider $\alpha = 1$ in this case, and $\alpha < 1$ otherwise. Considering $\alpha = 1$ for S measurements performed on the Mn_5Ge_3 films under external magnetic field (Fig. 3b and Table 1), we obtain $\alpha = ½$ without magnetic field, which is coherent with the considered model. The product $\beta\Delta E_{eI} = 0.02$ eV

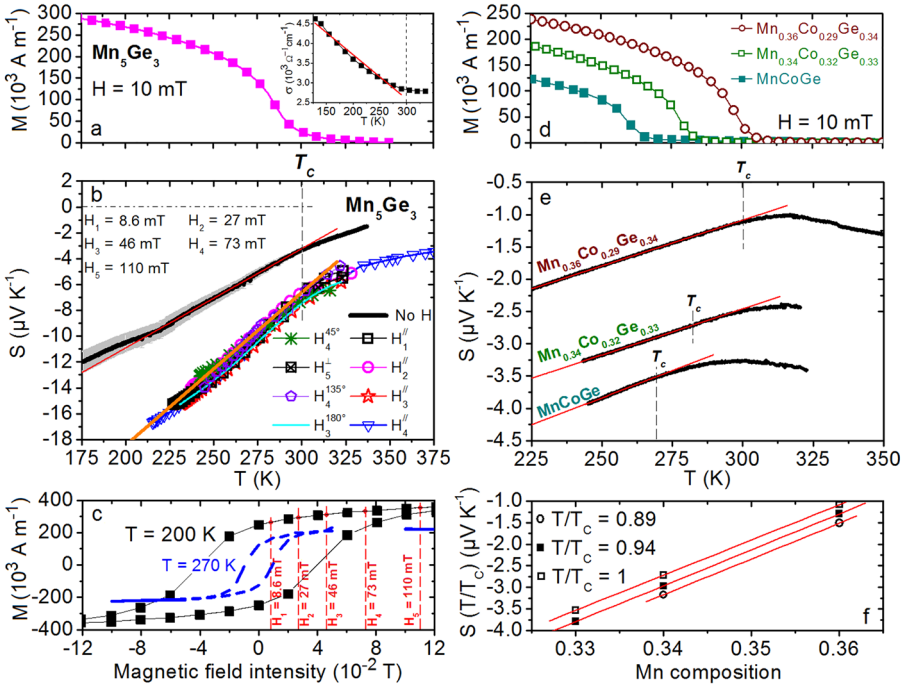

Figure 3. Magnetization (M) and Seebeck coefficient (S) measurements performed on Mn_5Ge_3 and MnCoGe thin films. M (**a**) and S (**b**) of a 50 nm-thick Mn_5Ge_3 film as a function of temperature. The inset in (**a**) presents the electrical conductivity of the film versus temperature. (**c**) M measured at 200 K (black solid squares) and 270 K (blue dashed line) on a same Mn_5Ge_3 film as a function of in-plane magnetic field intensity. M (**d**) and S (**e**) of 150 nm-thick $Mn_xCo_yGe_{1-x-y}$ films as a function of temperature. (**f**) $S(T/T_c)$ of same $Mn_xCo_yGe_{1-x-y}$ films plotted as a function of Mn composition x.

		A (eV)	B
Mn_5Ge_3	$H=0$	0.005	−0.16
	$H=H_{SAT}$	0.01	−0.30
MnCoGe	$H=0$	0.001	−0.008
$Mn_{0.34}Co_{0.32}Ge_{0.33}$	$H=0$	0.001	−0.011
$Mn_{0.36}Co_{0.29}Ge_{0.34}$	$H=0$	0.001	−0.022

Table 1. Parameters A and B in Eq. (4) determined experimentally from S measurements presented in Fig. 3b for Mn_5Ge_3 films and Fig. 3e for $Mn_xCo_yGe_{1-x-y}$ films.

at magnetization saturation. For comparison, the coupling energy of the localized moments should be of the order of $k_BT_c = 0.026$ eV (Fig. 3a). Comparing the values of B with and without external magnetic field (Table 1), the scattering parameter ΔR_{SAT} ($H = H_{SAT}$) is found to be twice as ΔR_0 ($H = 0$), with $\Delta R_0/\Delta R_{SAT} \sim ½ < 1$. This means that the relaxation time difference $\Delta\tau$ between minority- and majority-spin electrons increases under magnetic field, and is found to scale with the parameter α in Mn_5Ge_3. These results agree with a higher polarization of conduction electrons at magnetization saturation. The polarization of free carriers has two opposite effects on the spin-dependent S: localized moment ordering promotes (i) an increase of $A = \beta\alpha\Delta E_{el}/2$ due to a statistical increase of $\boldsymbol{s_e}$ and $\boldsymbol{\mu_I}$ pairing, increasing S, and (ii) an increase of $\Delta\tau$, decreasing S. However, the global effect of localized magnetic moment ordering in FM Mn_5Ge_3 promotes the increase of S at given T. $\boldsymbol{H}$ effect agrees with thermal fluctuation effect, as in the two cases, the spin-dependent S increases with localized moment polarization. This behavior can be the signature of bipolar conduction, since in the case of a FM film containing a single moment $\boldsymbol{\mu_I}$, $M = (n^+ - n^-)\mu_I$ with n^+ and n^- the concentrations of occupied states in each level (up and down).

Magnetic moment density. Figure 2a presents three diffractograms (b), (c), and (d), acquired on three MnCoGe films of different Mn composition. The films contain only the hexagonal MnCoGe phase (Supplementary Fig. S1b). They are polycrystalline and composed of columnar grains with a thickness ~ 152 ± 5 nm. The RMS surface roughness is ~ 0.9 nm and the MnCoGe grains exhibit an average lateral size ~ 1.8 × 0.7 μm² for the three films MnCoGe, $Mn_{0.34}Co_{0.32}Ge_{0.33}$, and $Mn_{0.36}Co_{0.29}Ge_{0.34}$ according to AFM measurements (Fig. 2b).

Figure 3d shows the magnetization variations versus temperature of the three $Mn_xCo_yGe_{1-x-y}$ films. Magnetization and Curie temperature increase with x, which correspond to an increase of the density of localized moment $\boldsymbol{\mu_I}$ and to an increase of the exchange energy between $\boldsymbol{\mu_I}$, respectively. Figure 3e presents the variations versus temperature of the spin-dependent S of the same films. Similar to Mn_5Ge_3, S is negative (n-type) and decreases linearly as temperature increases up to T_c for the three films. The FM/PA transition is more easily detected in the case of MnCoGe films, especially for $Mn_{0.36}Co_{0.29}Ge_{0.34}$, S increasing with temperature after T_c. This change of behavior of S versus T is commonly observed in FM metals, S variations resulting from the bipolar effect of spin-up and spin-down electrons before T_c and S following the behavior of common metals after T_c [53]. Furthermore, S is found to decrease as the Mn concentration increases in the MnCoGe films. The parameters A and B in Eq. (4) were determined from S measurements presented in Fig. 3e. They are displayed in Table 1. The slope of the linear function $S=f(T)$ is independent of the Mn concentration with $A=0.001$ eV for the three samples (Table 1), giving $\beta\alpha\Delta E_{eI}=0.002$ eV if $\Delta E_C=0$ in Eq. (3). This result suggests that the 3 at% increase of Mn atoms in the compound MnCoGe does not involve a significant modification of the MnCoGe DOS close to E_F in our temperature range, supporting a constant parameter β, independent of Mn concentration. Furthermore, constant $\alpha\Delta E_{eI}$ suggests also that the increase of exchange energy between localized moments $\boldsymbol{\mu_I}$ has no influence on the average coupling energy of the conduction electron spin $\boldsymbol{s_e}$ with $\boldsymbol{\mu_I}$. Figure 3f presents S variations versus the Mn composition of $Mn_xCo_yGe_{1-x-y}$ films. S is inversely proportional to x. This behavior is the result of the linear decrease of the parameter B as x increases in $Mn_xCo_yGe_{1-x-y}$ films (Fig. 4a), suggesting an increase of $\Delta\tau$ with Mn concentration (Tab. 1), which is in agreement with the electrical conductivity behavior of $Mn_xCo_yGe_{1-x-y}$ films versus x. Indeed, Fig. 4b shows that σ decreases as x increases. $\sigma=en\mu_e$ can decrease either due to a decrease of carrier density n, or due to a decrease of carrier mobility μ_e.

However, β being independent of Mn concentration, the linear decrease of S versus x appears to be related to a decrease of $\mu_e=e\tau/m^*$, due to a modification of the average scattering time τ in the two spin-dependent channels, resulting from a scattering effect associated with the additional Mn atoms. The increase of the magnetic moment density in MnCoGe have negligible effect on the exchange energy between conduction electron spin and localized $\boldsymbol{\mu_I}$, but promotes an increase of $\Delta\tau$, leading to the decrease of S.

Extra Mn ions can act as additional spin-dependent scattering centers[50], supporting a stronger spin-dependent scattering, which should be accompanied with a higher polarization of free electrons[50]. However, the polarization increase is not observed on the slope of the linear function $S=f(T)$, such as in the case of Mn_5Ge_3 films under external magnetic field (Fig. 3b). $\Delta\tau$ could also be related to conduction electron bipolarity. Indeed, in the case of bipolar conduction, majority-spin electrons should diffuse towards the cold side (n-type S), while minority-spin electrons should diffuse towards the hot side, which could explain a difference of scattering conditions in the two channels independent of α. The decrease of S with the increase of Mn concentration should not be related to the corresponding polarization increase (Fig. 3d), since the spin-dependent S is observed to increase with magnetic polarization in both Mn_5Ge_3 (Fig. 3b) and $Mn_xCo_yGe_{1-x-y}$ (Fig. 3e). Instead, the decrease of S with the increase of x is related to the corresponding increase of the direct exchange energy $E_{ex}=-J_{ex}\boldsymbol{\mu_I}.\boldsymbol{\mu_I}$ between Mn magnetic moments. Since $\boldsymbol{\mu_I}$ coupling vanishes at $T=T_c$, $E_{ex}\sim k_BT_c$ can be assumed. The insert in Fig. 4a presents

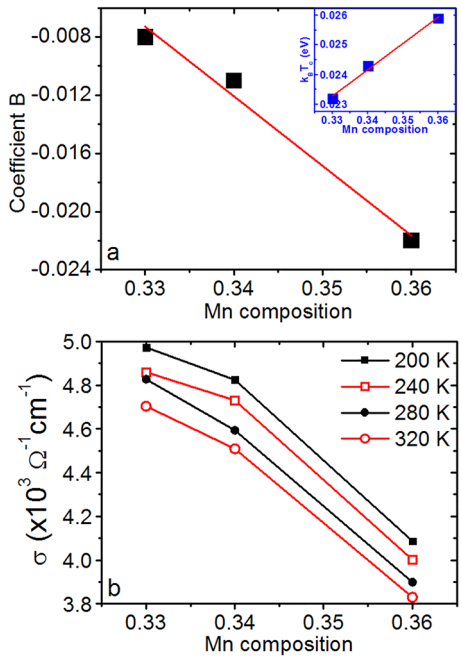

Figure 4. Electrical properties of the $Mn_xCo_yGe_{1-x-y}$ thin films. (**a**) electron-scattering-dependent parameter B (Eq. 4) as a function of x. The inset shows the k_BT_c energy variation versus x. (**b**) Electrical conductivity as a function of x, measured at different temperatures.

the variations of the product $k_B T_c$ versus x. E_{ex} is found to increase linearly with the Mn content. Consequently, free electron scattering in FM MnCoGe mainly involves coupled Mn magnetic moments, explaining the linear increase of the spin-dependent scattering difference (ΔR in Eq. 3) between the two spin-dependent channels with Mn composition by the linear increase of moments' exchange energy.

Outlook. The influence of thermal fluctuations, ordering, and density of localized magnetic moments on the spin-dependent Seebeck coefficient S has been investigated in ferromagnetic Mn_5Ge_3 and MnCoGe thin films. S is found to be mainly sensitive to the polarization of the conduction electrons, according to two opposite mechanisms: (i) the coupling of the spin vector of free carriers with the localized moments leads to higher S, while (ii) an increase of the scattering difference in the two spin-dependent conduction channels leads to lower S. In the case of Mn_5Ge_3 films under external magnetic field, the overall contribution of the two mechanisms leads to an increase of S. The thermal fluctuations of localized magnetic moments, as well as moment ordering using an external magnetic field show coherent effects, as in both cases S increases with localized moment polarization. The increase of Mn concentration in hexagonal MnCoGe leads to an increase of the magnetic moment density and of the localized moment exchange energy. The moment density increase is found to have no effect on the average exchange energy between the spin of conduction electrons and localized moments, but promotes an increase of the relaxation time difference between the two spin-dependent conduction channels, leading to the linear decrease of S as the Mn content increases. Our observations in model materials coupled with the expression proposed in Eq. (3) open prospects for original engineering routes for the development of spin-engineered thermoelectric materials.

Materials and methods

Mn_5Ge_3 and MnCoGe films were elaborated by magnetron sputtering and solid-state reaction. 99.99% pure Co, 99.99% pure Ge, and 99.9% pure Mn targets were sputtered on 1.5×2.5 cm^2 glass substrates in a commercial magnetron sputtering system with a base vacuum of 10^{-8} Torr[28]. In this system, three targets placed at an angle of 45° to the normal of the sample surface can be simultaneously sputtered during the substrate rotation. Co, Ge, and Mn deposition rates were separately calibrated thanks to the measurement by X-ray reflectivity (XRR) of the thickness of different films deposited in different conditions. The substrates were cleaned 10 min in an acetone bath before to be rinsed 10 min in alcohol in an ultrasonic cleaner. They were finally kept 30 min at 423 K in a baking furnace, before to be loaded in the sputtering chamber. The elements were deposited (Ge and Mn for Mn_5Ge_3) or co-deposited (Mn, Co, and Ge for MnCoGe) at room temperature on the glass substrates that were rotated at 5 rpm. The Mn_5Ge_3 films were produced by reactive diffusion: 35 nm of Ge were deposited on the glass substrate before to be capped with 31 nm of Mn[30]. After deposition, the samples were ex situ annealed under vacuum ($P \sim 10^{-7}$ mbar) at 400 °C for 10 min. The diffractogram (a) in Fig. 2a shows some diffraction peaks belonging to the Ge lattice in addition to the peaks of the phase Mn_5Ge_3, meaning that the Ge layer was not entirely consumed by the growth of Mn_5Ge_3 despite the entire consumption of the Mn layer. The MnCoGe films were produced by non-diffusive reaction[28], allowing the stoichiometry of the compound to be varied: Mn, Co, and Ge were co-sputtered on the substrate up to a thickness of 150 nm. The samples were also ex situ annealed at 400 °C for 10 min after deposition.

Sample structure was investigated by both X-ray diffraction (XRD) in the Bragg–Brentano geometry ($\theta - 2\theta$) using a Cu K_α source ($\lambda_{K\alpha} = 0.154$ nm) in a PANalytical X'Pert PRO setup equipped with an X'Celerator detector, and by atomic force microscopy (AFM) using a Solver-PRO system from NT-MDT. Film magnetization was measured versus temperature using a SQUID magnetometer Quantum Design MPMSXL. Hall measurements and sample resistivity were measured in the Van der Pauw geometry using a lab-made setup operating between 20 and 350 K. The applied magnetic field for Hall measurements was 0.5 T. The Seebeck coefficients of the films were measured using a home-made setup[39] between $T = 225$ and 325 K, close to the FM/PM transition, according to the geometry presented in Fig. 1a. The distance d between the two electrodes was 1 cm.

Data availability

All data are available in the main text or the supplementary materials.

Received: 3 October 2022; Accepted: 22 December 2022
Published online: 04 January 2023

References

1. Tu, S. *et al.* Record thermopower found in an IrMn-based spintronic stack. *Nat. Commun.* **11**, 1–7 (2020).
2. Davids, P. S. *et al.* Electrical power generation from moderate-temperature radiative thermal sources. *Science (80-).* **367**, 1341–1345 (2020).
3. Wang, Y., Guo, T., Tian, Z., Bibi, K., Zhang, Y., Alshareef, H. N. MXenes for energy harvesting. *Adv. Mater.* 2108560 (2022).
4. Hu, G., Edwards, H. & Lee, M. Silicon integrated circuit thermoelectric generators with a high specific power generation capacity. *Nat. Electron.* **2**, 300–306 (2019).
5. Dhawan, R. *et al.* $Si_{0.97}Ge_{0.03}$ microelectronic thermoelectric generators with high power and voltage densities. *Nat. Commun.* **11**, 4362 (2020).
6. He, J. & Tritt, T. M. Advances in thermoelectric materials research: Looking back and moving forward. *Science (80-).* https://doi.org/10.1126/science.aak9997 (2017).
7. Miao, J. *et al.* Modulated carrier concentration and enhanced seebeck coefficient of Ge2Sb2Te5 thin films by Sn doping. *Vacuum* **198**, 110881 (2022).
8. Peng, Y. *et al.* Constructed Ge quantum dots and Sn precipitate SiGeSn hybrid film with high thermoelectric performance at low temperature region. *Adv. Energy Mater.* https://doi.org/10.1002/aenm.202103191 (2022).

9. Heremans, J. P. *et al.* Enhancement of thermoelectric efficiency in PbTe by distortion of the electronic density of states. *Science (80-).* **321**, 554–557 (2008).
10. Zheng, J. *et al.* Synergistically enhanced thermoelectric properties in n-type Bi 6 Cu 2 Se 4 O 6 through inducing resonant levels. *Acta Mater.* **232**, 117930 (2022).
11. Narducci, D., Selezneva, E., Cerofolini, G., Frabboni, S. & Ottaviani, G. Impact of energy filtering and carrier localization on the thermoelectric properties of granular semiconductors. *J. Solid State Chem.* **193**, 19–25 (2012).
12. Puneet, P. *et al.* Preferential scattering by interfacial charged defects for enhanced thermoelectric performance in few-layered n-type Bi 2 Te 3. *Sci. Rep.* **3**, 1–7 (2013).
13. Zhang, X. *et al.* Significant enhancement in thermoelectric properties of half-Heusler compound TiNiSn by grain boundary engineering. *J. Alloys Compd.* **901**, 163686 (2022).
14. Mao, J., Liu, Z. & Ren, Z. Size effect in thermoelectric materials. *NPJ Quantum Mater.* **1**, 1–9 (2016).
15. Santos, R., Nancarrow, M., Dou, S. X. & Aminorroaya Yamini, S. Thermoelectric performance of n-type Mg2Ge. *Sci. Rep.* **7**, 1–7 (2017).
16. Dhawan, R. *et al.* Si0.97Ge0.03 microelectronic thermoelectric generators with high power and voltage densities. *Nat. Commun.* **11**, 1–8 (2020).
17. Wang, A. *et al.* High thermoelectric performance of Cu2Se-based thin films with adjustable element ratios by pulsed laser deposition. *Mater. Today Energy.* **24**, 100929 (2022).
18. Narducci, D. & Giulio, F. Recent advances on thermoelectric silicon for low-temperature applications. *Materials (Basel).* **15**, 1–13 (2022).
19. Adachi, H., Uchida, K. I., Saitoh, E. & Maekawa, S. Theory of the spin Seebeck effect. *Rep. Prog. Phys.* https://doi.org/10.1088/0034-4885/76/3/036501 (2013).
20. Uchida, K. *et al.* Observation of the spin Seebeck effect. *Nature* **455**, 778–781 (2008).
21. Jaworski, C. M. *et al.* Observation of the spin-Seebeck effect in a ferromagnetic semiconductor. *Nat. Mater.* **9**, 898–903 (2010).
22. Kirihara, A. *et al.* Spin-current-driven thermoelectric coating. *Nat. Mater.* **11**, 686–689 (2012).
23. Johari, K. K., Bathula, S. & Gahtori, B. The role of magnetic interaction on the thermoelectric performance of ZrNiSn half-Heusler alloys. *Phys. Status Solidi.* **219**, 2100765 (2022).
24. Tu, S. *et al.* Record thermopower found in an IrMn-based spintronic stack. *Nat. Commun.* **11**, 2023 (2020).
25. Mersal, G. A. M. *et al.* Study of half metallic ferromagnetism and thermoelectric properties of spinel chalcogenides BaCr2X4 (X = S, Se, Te) for spintronic and energy harvesting. *J. Mater. Res. Technol.* **18**, 2831–2841 (2022).
26. Lin, W. *et al.* Giant spin-dependent thermoelectric effect in magnetic tunnel junctions. *Nat. Commun.* **3**, 744 (2012).
27. Fortulan, R. *et al.* Thermoelectric performance of n-type magnetic element doped Bi2S3. *ACS Appl. Energy Mater.* https://doi.org/10.1021/acsaem.2c00295 (2022).
28. Tsujii, N., Nishide, A., Hayakawa, J. & Mori, T. Observation of enhanced thermopower due to spin fluctuation in weak itinerant ferromagnet. *Sci. Adv.* **5**, 1–9 (2019).
29. Tawara, Y. & Sato, K. On the magnetic anisotropy of single crystal of Mn 5 Ge 3. *J. Phys. Soc. Jpn.* **18**, 773–777 (1963).
30. Forsyth, J. B. & Brown, P. J. The spatial distribution of magnetisation density in Mn 5 Ge 3. *J. Phys. Condens. Matter.* **2**, 2713–2720 (1990).
31. Picozzi, S., Continenza, A. & Freeman, A. J. First-principles characterization of ferromagnetic Mn5Ge 3 for spintronic applications. *Phys. Rev. B Condens. Matter Mater. Phys.* **70**, 1–10 (2004).
32. Panguluri, R. P. *et al.* Spin polarization and electronic structure of ferromagnetic Mn 5Ge3 epilayers. *Phys. Status Solidi Basic Res.* **242**, 67–69 (2005).
33. Spiesser, A. *et al.* Effect of thickness on structural and magnetic properties of Mn5Ge3 films grown on Ge(111) by solid phase epitaxy. *Thin Solid Films* **518**, S113–S117 (2010).
34. Deng, S., Heid, R., Bohnen, K. P., Wang, C. & Sürgers, C. Minority-spin conduction in ferromagnetic Mn5Ge3 Cx and Mn5Si3 Cx films derived from anisotropic magnetoresistance and density functional theory. *Phys. Rev. B.* **103**, 1–6 (2021).
35. Jeitschko, W. A high-temperature X-ray study of the displacive phase transition in MnCoGe. *Acta Crystallogr. Sect. B Struct. Crystallogr. Cryst. Chem.* **31**, 1187–1190 (1975).
36. Kaprzyk, S. & Niziol, S. The electronic structure of CoMnGe with the hexagonal and orthorhombic crystal structure. *J. Magn. Magn. Mater.* **87**, 267–275 (1990).
37. Lin, S. *et al.* Structural and magnetic properties of MnFe$_1 - rm x$Co$_rm x$Ge Compounds. *IEEE Trans. Magn.* **42**, 3776–3778 (2006).
38. Wang, J.-T. *et al.* Vacancy induced structural and magnetic transition in MnCo1−xGe. *Appl. Phys. Lett.* **89**, 262504 (2006).
39. Wang, Z. *et al.* First-order magnetostructural transformation in Fe doped Mn–Co–Ge alloys. *J. Alloys Compd.* **577**, 486–490 (2013).
40. Si, X. *et al.* Enhancement of Curie temperature and transition temperature range induced by Al doping in Mn1-xAlxCoGe. *Solid State Commun.* **247**, 27–30 (2016).
41. Hahn, K. R., Assaf, E., Portavoce, A., Bertaina, S. & Charaï, A. Structural and composition effects on electronic and magnetic properties in thermoelectric Mn1-x-yCo1+xGe1+y materials. *J. Phys. Chem. C.* **121**, 26575–26586 (2017).
42. Portavoce, A. *et al.* Ferromagnetic MnCoGe thin films produced via magnetron sputtering and non-diffusive reaction. *Appl. Surf. Sci.* **437**, 336–346 (2018).
43. Assaf, E. *et al.* Structural and magnetic properties of MnCoGe ferromagnetic thin films produced by reactive diffusion. *Appl. Surf. Sci.* **488**, 303–315 (2019).
44. Assaf, E., Portavoce, A., Hoummada, K., Bertoglio, M. & Bertaina, S. High Curie temperature Mn5Ge3 thin films produced by non-diffusive reaction. *Appl. Phys. Lett.* https://doi.org/10.1063/1.4976576 (2017).
45. Chambers, R. G. Transport properties of semiconductors. *Electron. Met. Semicond.* 186–202 (1990).
46. Herring, C. Theory of the thermoelectric power of semiconductors. *Phys. Rev.* **96**, 1163 (1954).
47. Fritzsche, H. A general expression for the thermoelectric power. *Solid State Commun.* **9**, 1813–1815 (1971).
48. Holzwarth, U. & Gibson, N. The Scherrer equation versus the "Debye-Scherrer equation". *Nat. Nanotechnol.* **6**, 534–534 (2011).
49. Assaf, E., Portavoce, A., Descoins, M., Bertoglio, M. & Bertaina, S. Carbon concentration, Curie temperature, and magnetic resonance field of Mn5Ge3(C) thin films. *Materialia.* **8**, 100487 (2019).
50. Seemann, K. M., Hickey, M. C., Baltz, V., Hickey, B. J. & Marrows, C. H. Spin-dependent scattering and the spin polarization of a diffusive current in partly disordered L10 epitaxial FePd. *New J. Phys.* **12**, 1–19 (2010).
51. Marrows, C. H. Spin-polarised currents and magnetic domain walls. *Adv. Phys.* **54**, 585–713 (2005).
52. Wegrowe, J. *et al.* Spin-dependent scattering of a domain wall of controlled size. *Phys. Rev. B Condens. Matter Mater. Phys.* **61**, 12216–12220 (2000).
53. Abadlia, L., Gasser, F., Khalouk, K., Mayoufi, M. & Gasser, J. G. New experimental methodology, setup and LabView program for accurate absolute thermoelectric power and electrical resistivity measurements between 25 and 1600 K: Application to pure copper, platinum, tungsten, and nickel at very high temperatures. *Rev. Sci. Instrum.* **85**, 095121 (2014).

Acknowledgements

The authors thank Voicu Dolocan for helpful discussions.

Author contributions

A.P.: Conceptualization, methodology, visualization, funding acquisition, project administration, supervision, writing—original draft, writing—review and editing. E.A.: Investigation. M.B.: Investigation, resources. D.N.: Investigation, writing—review and editing. S.B.: Conceptualization, funding acquisition, supervision, writing—review and editing.

Funding

This work was supported by the French government through the program "Investissements d'Avenir A*MIDEX" (Project APODISE, no. ANR-11-IDEX-0001-02).

Competing interests

The authors declare no competing interests.

Additional information

Supplementary Information The online version contains supplementary material available at https://doi.org/10.1038/s41598-022-26993-3.

Correspondence and requests for materials should be addressed to A.P.

Reprints and permissions information is available at www.nature.com/reprints.

Publisher's note Springer Nature remains neutral with regard to jurisdictional claims in published maps and institutional affiliations.